Renewable Energy 195 (2022) 637–647

Contents lists available at ScienceDirect

Renewable Energy

journal homepage: www.elsevier.com/locate/renene

Flow effects of finite-sized tidal turbine arrays in the Chacao Channel, Southern Chile

Karina Soto-Rivas [a, b, c], David Richter [b], Cristian Escauriaza [a, c, *]

[a] Departamento de Ingeniería Hidráulica y Ambiental, Pontificia Universidad Católica de Chile, Av. Vicuña Mackenna 4860, 7820436, Santiago, Chile
[b] Department of Civil and Environmental Engineering and Earth Sciences, University of Notre Dame, Notre Dame, IN, 46556, USA
[c] Marine Energy Research & Innovation Center (MERIC), Av. J. E. de Balaguer 13105, Of. 1011, Lo Barnechea, Santiago, Chile

ARTICLE INFO

Article history:
Received 10 December 2021
Received in revised form
5 May 2022
Accepted 28 May 2022
Available online 20 June 2022

Keywords:
Marine energy
FVCOM
MHK devices

ABSTRACT

To characterize energy resources and study of hydrodynamic effects induced by marine hydrokinetic devices in tidal channels, numerical models need to provide reliable representations of turbine arrays. In regions disconnected from the grid, near coastal protected areas and other relevant economic activities, there is a pressing need to evaluate the impacts of limited-size arrays. Here, we use the emblematic Chacao Channel in Southern Chile to understand the effects of bathymetry and array placement on energy extraction in strongly tidal channels. We implement in FVCOM a parameterization from a previously derived high-resolution model to represent a group of turbines in different locations. We first analyze the complexity of the bathymetry to define the appropriate grid size and obtain a correct representation of the interaction of turbines with the bed morphology. We simulate a base case to identify three suitable locations in the channel where we analyze the effects of the turbines: From simulations we compute the changes in the mean velocity, turbulent kinetic energy (TKE), and bed shear stress. The results show that baseline velocities and TKE are the main factors on the momentum extraction despite the bed complexity. However, in flatter bathymetries, changes on TKE and bottom shear are significantly larger compared to complex morphologies, since turbine arrays modify considerably the original flow conditions. Simulations also provide additional insights that are critical to evaluate the local impacts, showing the directionally-dependent flow resistance of tidal channels, in which the interactions with bathymetry change the downstream effects of turbine arrays in flood or ebb regimes.

1. Introduction

The use of marine hydrokinetic (MHK) devices for extracting tidal energy has become an attractive alternative to alleviate the ever-increasing world energy demand [1–3]. In many coastal regions, tidal energy offers advantages over other renewable sources, since it is predictable with minimal visual impacts [4–6]. However, there are still multiple technical and environmental challenges that current technologies will have to address, specially when analyzing the flow impacts produced by the deployment of finite-sized arrays. Previous investigations on the effects of turbine arrays in tidal channels have mostly considered large-scale farms, which are typically designed to be connected to the grid [7,8]. Initial developments in the South Pacific Ocean, in the coast of Chile, will focus first on small-scale installations to supply isolated areas with the objective of reducing emissions and contributing to achieve the national commitments toward carbon neutrality [9].

The Chacao Channel (41°47′S, 73°32′W), which connects the Pacific Ocean with the interior fjords in the south of Chile, stands out in the region due to its tidal energy potential with flow velocities that reach over 4 m/s [10]. This site is a characteristic example of a tidal channel with a complex ecosystem and conflicting human activities, where the assessment of the impacts produced by installing a finite-sized MHK farm is critical to understand the effects on physical habitats and local hydrodynamics. Changes on flow acceleration, bottom shear, and increases on turbulent kinetic energy (TKE) induced by turbines can modify sediment transport patterns and modulate the local morphodynamics [11,12].

Numerical simulations in ocean circulation models (OCM)

* Corresponding author. Departamento de Ingeniería Hidráulica y Ambiental, Pontificia Universidad Católica de Chile, Av. Vicuña Mackenna 4860, 7820436, Santiago, Chile.
E-mail addresses: knsoto@uc.cl (K. Soto-Rivas), David.Richter.26@nd.edu (D. Richter), cescauri@ing.puc.cl (C. Escauriaza).

https://doi.org/10.1016/j.renene.2022.05.150
0960-1481/

represent MHK devices by implementing a parameterization of turbine arrays, modifying the flow resistance coefficients or adding a sink of momentum in the governing equations of the flow. Both approaches have been considered in two-dimensional (2D) models, increasing bed friction [13,14], or applying a momentum sink to represent different turbine separations by changing the device density (i.e., numbers of devices per unit area) in the grid elements [15,16]. In three-dimensional (3D) simulations, on the other hand, increasing the bed friction [17] might not capture the effects of the turbine arrays as the vertical position of the devices is not considered. The momentum sink approach has been successfully implemented in 3D models such as ROMS [18], which was used by Ref. [19] to represent MHK devices on a flat channel, and later by Ref. [20] on a realistic bathymetry. The 3D model FVCOM [21], which considers unstructured elements to adapt the grid to the coastline, has also been employed with the momentum sink approach to represent MHK devices over flat bathymetries [22] and in natural conditions [23–25]. Models of MHK devices in real marine environments using OCMs, however, typically simulate an unrealistic number of turbines that exceed hundreds or even thousands of units [7,13,22].

These previous formulations cannot be applied when a small number of devices interact with the flow in finite-sized arrays, in cases where changes in the resistance force or momentum caused by different turbine distributions are relevant. This problem can be solved by representing just one turbine per grid cell, but in that case, the location of the devices is restricted by the grid resolution of the computational domain and the bathymetric data. Considering the distribution of the devices in larger-scale models with simplified representations is essential to capture their effects on the local environment, since depending on their distance and relative positions, the velocities can change in direction and magnitude, producing also more efficient configurations than others [26,27].

In this work, we use numerical simulations to represent a finite-sized farm of MHK devices in the Chacao channel to assess their effects on the local physical environment. To represent the interactions between the tidal current and the bathymetry, we use the FVCOM model and incorporate a new momentum sink approach [28] to the MHK module developed by O'hara et al. [23]. Turbines are represented at larger scales by considering a localized force, and the effects of the turbine array are represented by a thrust coefficient, C_{tFarm}, which considers the lateral separation and the number of rows of MHK devices for a staggered distribution of turbines. To select the location of the installation site, we study the undisturbed conditions in the Chacao channel and compute the viable zones depending on the local velocities, according to the ranges of operation of commercial devices. After choosing the location of the farm, we analyze the local bathymetry using the variogram method [29] to design an appropriate numerical grid that can resolve the essential features of the bed and relate them to the flow/turbine interactions. Finally, we evaluate how tides and different local bathymetries interact with the finite-sized farms. In particular, we observe changes in the streamwise velocity, TKE, and shear stresses at the bed since they can produce significant impacts on the local environment, in line with our overall goal of assessing changes due to the installation of MHK turbine arrays in the Chacao channel.

2. Numerical simulations of MHK farms in the Chacao Channel

To simulate the tidal flow in the channel we use FVCOM, a 3D unstructured finite-volume hydrodynamic model that solves the primitive ocean circulation equations for mass, momentum, salinity, and temperature of the flow forced by tides, wind stress, and river discharges [21]. The governing equations for mass and momentum conservation solved in the x, y, and z directions (East, North, and vertical directions, respectively) can be written as follows:

$$\frac{\partial u}{\partial x}+\frac{\partial v}{\partial y}+\frac{\partial w}{\partial z}=0 \tag{1}$$

$$\frac{\partial u}{\partial t}+u\frac{\partial u}{\partial x}+v\frac{\partial u}{\partial y}+w\frac{\partial u}{\partial z}-fv= -\frac{1}{\rho}\frac{\partial P}{\partial x}-\frac{1}{\rho}\frac{\partial q_0}{\partial x}+\frac{\partial}{\partial z}\left(K_m\frac{\partial u}{\partial z}\right)+F_u \tag{2}$$

$$\frac{\partial v}{\partial t}+u\frac{\partial v}{\partial x}+v\frac{\partial v}{\partial y}+w\frac{\partial v}{\partial z}-fu= -\frac{1}{\rho}\frac{\partial P}{\partial y}-\frac{1}{\rho}\frac{\partial q_0}{\partial y}+\frac{\partial}{\partial z}\left(K_m\frac{\partial v}{\partial z}\right)+F_v \tag{3}$$

$$\frac{\partial w}{\partial t}+u\frac{\partial w}{\partial x}+v\frac{\partial w}{\partial y}+w\frac{\partial w}{\partial z}= -\frac{1}{\rho}\frac{\partial q_0}{\partial z}+\frac{\partial}{\partial z}\left(K_m\frac{\partial w}{\partial z}\right)+F_w \tag{4}$$

where u, v, and w are the velocities in the East, North, and vertical directions, respectively. The water column depth is the sum of the bottom depth and the free-surface height. f is the Coriolis parameter, F_u and F_v are the horizontal momentum diffusivity terms, P and q_0 are the hydrostatic and non-hydrostatic pressures, respectively, and K_m is the vertical eddy viscosity coefficient.

2.1. Model for finite-sized turbine arrays

To incorporate a finite-sized array of tidal turbines in the FVCOM simulations, we consider a streamwise momentum sink [30] in the governing equations of the flow to represent the devices [23], adding a force in Eq. (2) that accounts for the entire turbine farm, F_{tFarm}, as follows:

$$\frac{\partial u}{\partial t}+u\frac{\partial u}{\partial x}+v\frac{\partial u}{\partial y}+w\frac{\partial u}{\partial z}-fv= -\frac{1}{\rho}\frac{\partial P}{\partial x}-\frac{1}{\rho}\frac{\partial q_0}{\partial x}+\frac{\partial}{\partial z}\left(K_m\frac{\partial u}{\partial z}\right) +F_x-F_{tFarm}. \tag{5}$$

This force term represents the entire turbine array in the flow at large scales, and the device interactions within the array that cannot be resolved by the grid resolution in the OCM. In this investigation, we implement the new version of F_{tFarm} derived by Soto-Rivas et al. [28], based on the analysis of high-resolution simulations of staggered turbine arrays. High-fidelity numerical simulations validated with experimental data [28,31] are employed to inform large-scale models and derive expressions for the thrust coefficient that represents the integrated effects of a finite number of turbines, C_{tFarm}, which considers the turbine distribution in the farm as follows:

$$\frac{C_{tFarm}}{C_t'}=\begin{cases}\left(\beta\dfrac{D}{S_y}\right)+\gamma & ,\dfrac{L_x}{S_x}=2\\ \left[1-\exp\left(-\alpha\dfrac{S_x}{D}\right)\right]\left(\dfrac{D}{S_y}\right)+\zeta & ,\dfrac{L_x}{S_x}>2\end{cases} \tag{6}$$

Here, S_x and S_y are the separation distances between devices in the

streamwise and spanwise directions respectively; D is the diameter of the turbines represented as an actuator disk; L_x is the length of the farm in the streamwise direction, and L_x/S_x is the number of rows of devices that comprises the farm; finally $\beta = 0.39$, $\gamma = 0.72$, $\alpha = 0.25$, and $\zeta = 0.57$ are coefficients obtained from the spatial integration of the high-resolution simulation results [28]. Therefore, the force that represents the turbine array is:

$$F_{tFarm} = \frac{1}{2}\rho u^2 A_d C_{tFarm} N_t. \quad (7)$$

where A_d is the area of turbine rotor, assumed as an actuator disk; N_t is the total number of devices per grid cell. The magnitude of the streamwise velocity u corresponds to the instantaneous solution at the grid cell in the vertical layer where the turbines are located.

The orientation of the horizontal-axis turbines is considered in the main streamwise direction of the channel, as the East-West direction dominates the flow in all the sites where we evaluate the installation of arrays. It is important to note that we only modify the momentum conservation equation in the x-direction (Eq. (5)) since the coefficient C_{tFarm} was obtained by Ref. [28] has been tested and validated using a flow predominantly aligned to the turbine axis, where the lateral velocity, v, is negligible compared to u. Later, in section 4 below, we show that this assumption is valid for the Chacao channel because the flow is nearly parallel to the turbine arrays in all the locations we study the flow.

For the turbulence closure, we implement the Mellor-Yamada model [32]. Since we are interested in the far-wake effects of turbine arrays, we do not introduce additional modifications to the TKE equations of the turbulence closure, which would require additional parameterizations of the turbine effects on the velocity fluctuations and turbulence production [19,33].

3. Methodology

We perform numerical simulations for the extension of the Chacao channel of 18 km, shown as the zone highlighted in orange in Fig. 1. The domain is discretized with a total of 4,000 nodes in the horizontal directions and ten layers in the vertical direction. For the vertical discretization, we use the sigma-layer approach, which evenly divides the total depth. Each case shows the results of 45 simulation days between March and June 2012. The boundary conditions for the inlet and outlet of the channel are obtained from the entire domain shown in Fig. 1 using the one-way nesting option of FVCOM, since the velocity deficit effects produced by turbine arrays are recovered in these domains. Meanwhile, the larger domain boundary conditions are the tides provided by Ref. [10]. The model is built upon the validated FVCOM simulations of [10]. The bottom roughness is also defined through a characteristic scale $z_0 = 40$ mm, which corresponds to the value previously defined in the model for a resolution of 50 m in the Chacao Channel by this previous investigation.

In the previous analysis of the FVCOM results for this area and resolution by Ref. [10], measurements of tidal gauges and ADCP stations installed through the channel were compared with simulated tidal amplitudes and currents. Their results showed 95% confidence intervals in the amplitude replication of the M2 tidal component, and a relative difference of less than 10% time-averaged vertical profiles of horizontal speeds (for details on the model validation, the reader is referred to Ref. [10]).

3.1. Location of the turbine farms

The sites that are analyzed for the turbine array installations are selected using technical criteria that depend on the depths and velocities, excluding regions that are protected or exclusive for navigation and fishing activities, as shown in Fig. 2. We initially analyze the flow in the Chacao channel, simulating the current conditions without devices, to choose the most suitable locations to harness tidal energy using a finite-sized farm. The operational range of depths and velocities at the sites are selected by considering devices that have been already installed in similar environments [34,35]. We simulate turbines with a rotor diameter $D = 10$ m and a hub height $z_{hub} = 12$ m, which corresponds to the dimensions of a *Sabella* D10 turbine [34,36]. The cut-in and cut-out speeds are equal to 0.4 m/s and 4 m/s, respectively.

We analyze an area with depths between 40 m and 85 m, as shown in Fig. 2, showing the instantaneous minimum and maximum water depths in conditions without turbines and the location of the restricted zones in the channel enclosed by the dashed lines. The absolute values of the time-averaged velocities are shown in Fig. 3, which are also an indication of the mean available power. The flow is divided into two regimes: flood (where the flow goes from West to East) and ebb (directed from East to West). In Figs. 2 and 3, the gray regions are outside the depth and velocity angle limits.

According to the depth and velocity shown in Figs. 2 and 3, we select three different locations labeled as cases A, B, and C, as shown in Fig. 4. By choosing three sites for the arrays across the channel, we aim to compare the flow-farm interactions under the influence of different local conditions. The dimensions of each zone are determined by the area occupied by the turbine arrays, which are composed of 27 devices distributed in an efficient staggered form [37–39]. The separation between devices in the streamwise direction is equal to $5D$ (500 m), as proposed in the literature [40]. The lateral separation is equal to $4D$ (400 m), to avoid significant interactions among the wakes that can reduce the performance of the turbines [27]. With these parameters, the dimensions of each MHK zone are 300×200 m^2 as shown in Fig. 4.

3.2. Bathymetry characterization to evaluate the grid resolution

For each site A, B, and C, we first analyze the statistics of bed elevation in the local bathymetry. The resolution of the grid discretization of the OCM needs to capture accurately the relevant bathymetric features that interact with the turbine array. To better understand the minimum resolution required in our configuration, we employ the high-resolution bathymetric dataset of 10 m [10] to identify the dominant scales of the bed, by using the variogram method [29] in two dimensions. A variogram γ provides the degree of linear scale dependency of a field, and it is defined as half of the variance of the elevation difference between points, as follows:

$$\gamma(r) = \frac{1}{2N(r)} \sum_{i=1}^{N(r)} \sum_{j=i+1}^{N(r)} (Z_i - Z_j)^2 \quad (8)$$

where r is the distance between each pair of points, N is the total number of points in the domain, and Z is the surface elevation. In a log-log plot of r versus γ we can observe that for small r the variogram increases monotonically, meanwhile for $r > r_s$ the variogram converges to a saturated value, where r_s is a characteristic bedform length scale that can be understood as the length where the structures are correlated; i.e., the predominant wavelength of the bathymetry [41].

Fig. 5 shows the variogram calculated by using the high-resolution (10 m) bathymetry data in different directions for zones A, B, and C. For example, for cases A and B, the variograms in latitude 0° (East direction) show a length scale of around 150 m; however, after reaching the local maximum, we see an increase or decrease of the variograms, which is known as cyclicity [42], which

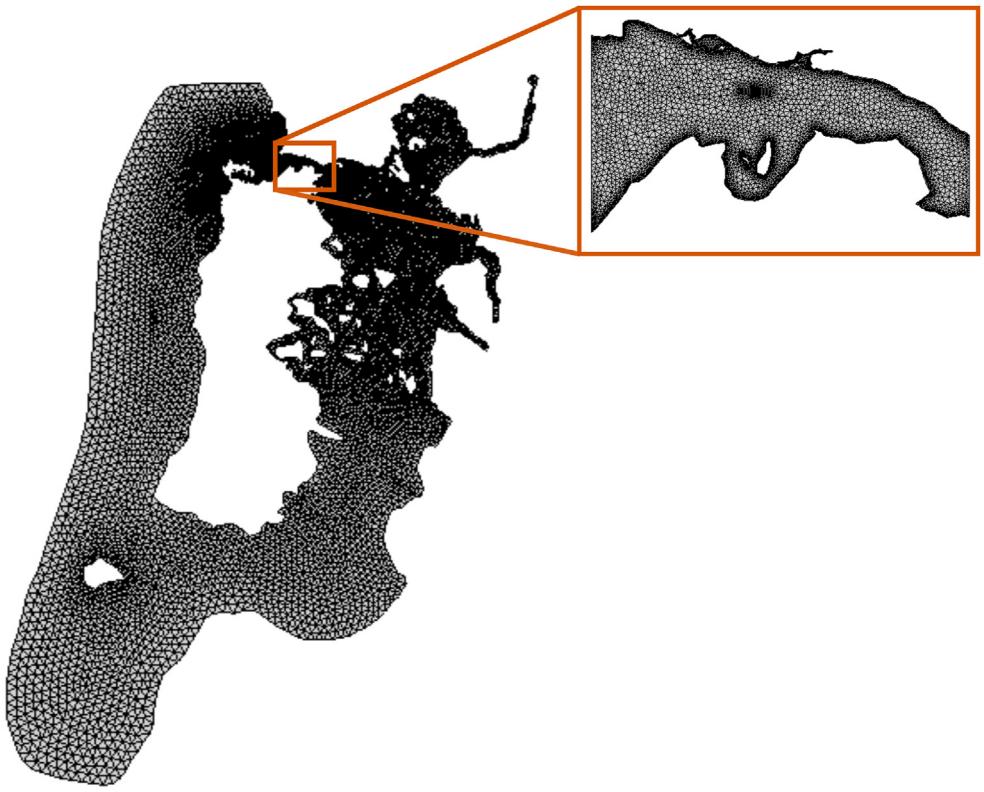

Fig. 1. Grid for the numerical simulations of the Chacao channel in FVCOM. The entire mesh surrounds the entire Chiloé island and is used to obtain the boundary conditions for the Chacao channel. Meanwhile, the zoom shows the domain we use for all the simulations, which has a higher resolution.

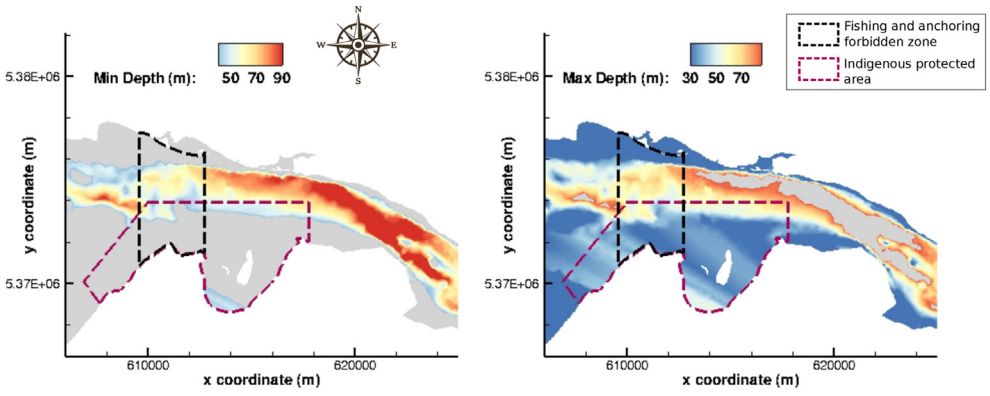

Fig. 2. Simulated minimum (left) and maximum (right) depth at every point through the time in the Chacao channel without turbines. Gray areas show the points where the minimum depth is under 40 m, and the maximum depth is over 85 m. Enclosed in dashed lines are the areas where the installation of MHK devices is restricted.

is an effect of the domain size that does not allow for the observation of larger dominant structures. In the other directions of cases A and B, there is no clear saturation value, which means the dominant wavelengths in those directions are larger than the size of the proposed array. In case C, we also observe cyclicity in the 30° and 60° directions; however, for 0°, we observe a dominant wavelength of around 150 m. Regarding the amplitude of bedforms, they are directly related to the variogram. Fig. 5 shows that the amplitude of case A is smaller than in case B, and they are both smaller than case C, as observed in the value of the variograms associated with the local, or global maxima corresponding to the dominant length scales.

Using this information, we design the computational grid of the channel incorporating the main scales of the local bathymetry. We ensure that the size of the discretization elements is equal to or smaller than 150 m, which was identified as the smaller dominant length scale of the bed in the variogram analysis (other examples of the use of variograms for defining the grid-size can be found in the works of [43,44]). At the top of Fig. 6 we show the FVCOM discretization of the entire domain with the high-resolution bathymetry data interpolated to the nodes. In the figure, we emphasize the elements we use around the turbine arrays, which are 100 m × 150 m (see Fig. 7).

At the bottom of Fig. 6, we show the high-resolution bathymetry with the interpolated bathymetry over the FVCOM grid in the longitudinal direction at the center span of zones A, B, and C. In the figure we show that with the computational grid we resolve the main bed features in the channel, and observe the small differences

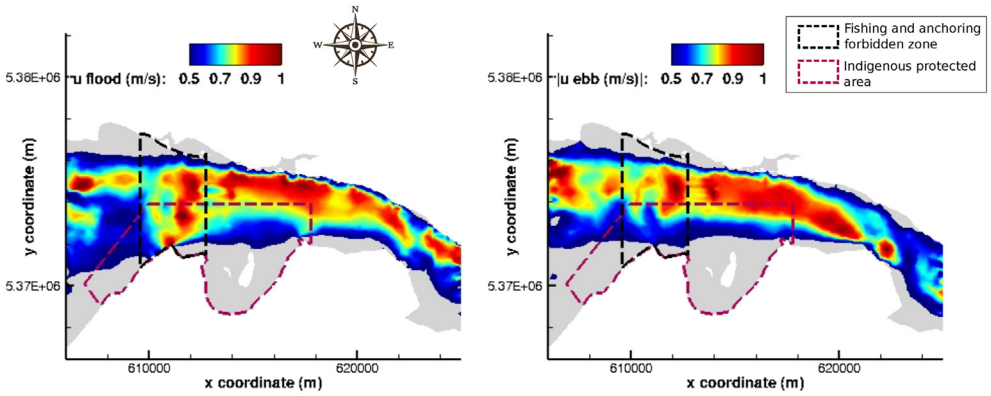

Fig. 3. Simulated absolute value of the time-averaged velocity at the hub height in the Chacao channel without turbines. Left: Ebb flow. Right: Flood flow. Gray areas show the points where the velocity is under 0.4 m/s and over 4.0 m/s. Enclosed in dashed lines are the areas where the installation of MHK devices is restricted.

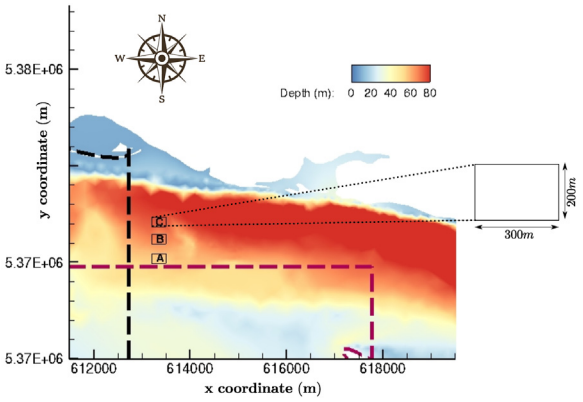

Fig. 4. Location of the arrays in the Chacao channel labeled as A, B, and C, and colored by the bathymetry. We also show a schematic of zone C dimensions, which are the same for zones A and B.

between the high-resolution (dashed lines) versus the grid resolution profiles (continuous lines). From these plots we can also interpret the variograms: for example, in cases A and B we can see that the bathymetry is nearly flat, which coincides with the fact that the bedform length-scales are more extensive than the farm size. However, in case B we observe larger bedforms than case A, showing also a larger local maximum in the variogram. Case C has larger fluctuations in the bed elevations, which are around 5 m (D/2); meanwhile, case B has fluctuations of 1 m amplitude (D/10) (see bottom of Fig. 6). The latter is consistent with the variogram that shows the largest amplitudes in latitude 0° for case C.

3.3. Simulation cases

The resolution of the computational grid is designed to resolve all the relevant bed features of the channel, based on the scale analysis of the bathymetry data shown in the previous section. The turbines are modeled using the actuator disk approach with the thrust coefficient obtained from the upscaled formulation [28], as presented in equation (6). A summary of the simulation inputs is presented in Table 1.

4. Results

We compare the flow in the Chacao channel without devices (case 0), to the cases with devices in finite-sized arrays (cases A, B, and C). We run each of the cases independently using the same computational grid and boundary and initial conditions. Here we present the changes in the velocity, modeled TKE, and bottom shear stresses produced by the turbines. We observe not only the effects in the flow inside the farms, but also the consequences of the

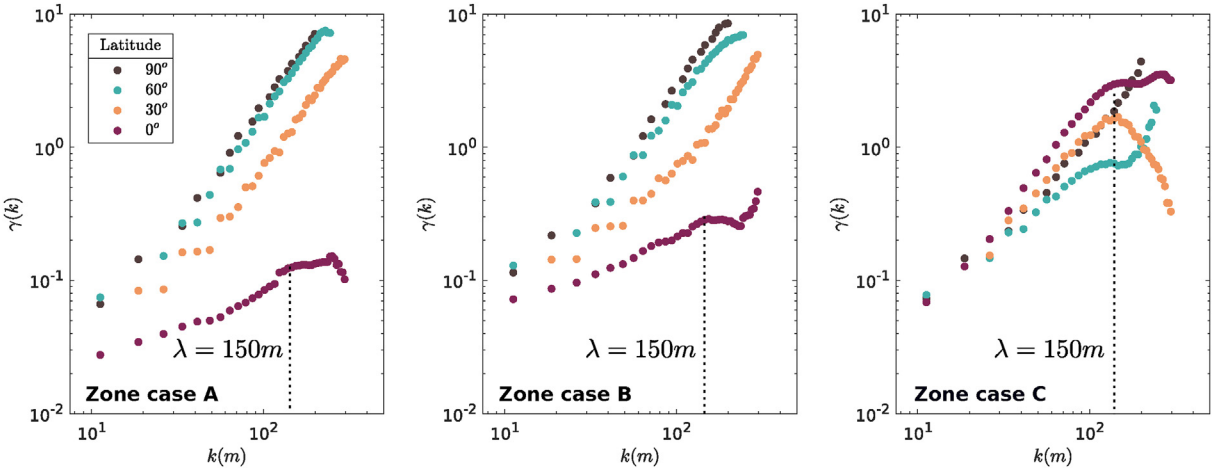

Fig. 5. Variograms of the bathymetry of the simulated cases in the Chacao channel (marked in Fig. 4), calculated in different directions, where 0° corresponds to the East direction, and 90°, to the North direction. The data set used for calculating them corresponds to the high-resolution bathymetric data (10 m).

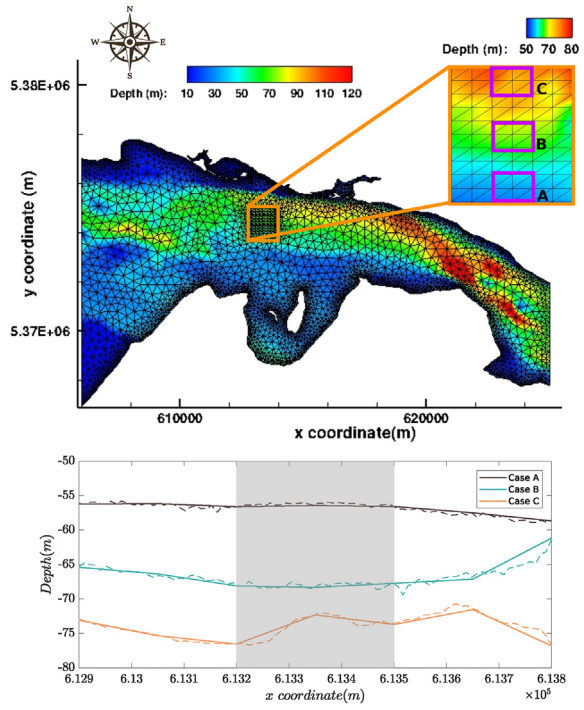

Fig. 6. Discretized computational domain for the simulations with turbines in FVCOM for the Chacao channel. Top: Domain colored by the interpolated high-resolution bathymetric data. The zoom highlights the area where the turbines are simulated; there, every element has a height of 100 m and a width of 150 m. The rectangles in purple indicate the exact area of zones A, B, and C. The legend at the left corresponds to the bathymetry of the entire domain; meanwhile, the legend at the right corresponds to the bathymetry of the zoomed area. Bottom: Bathymetry at the center-span of the zones of cases A, B, and C. The continuous lines are the bathymetry used for the simulations. The dashed lines are corresponded to the high-resolution bathymetry taken from Ref. [10] every 10 m. The zone occupied by the farms is marked in gray.

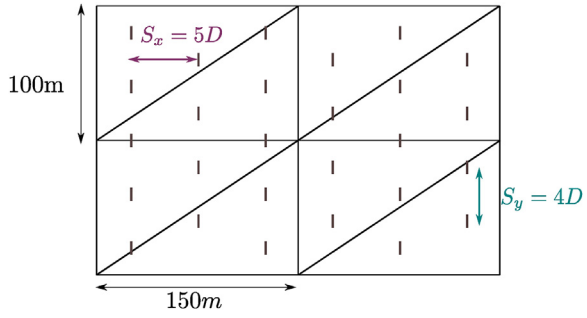

Fig. 7. Schematic of the turbine distribution for cases A, B, and C, where S_x is the distance between rows, and S_y is the lateral distance between the center of the disks. Black lines show the computational grid used in FVCOM for representing the farms, which are the same purples rectangles highlighted in the zoomed area of Figure.6.

turbines downstream. We also show how the theoretical power of the farms change according to their location in the channel.

4.1. Base conditions: Chacao channel simulations without turbines

To define the baseline conditions before analyzing the impacts of installing a finite array of turbines in the channel, we run numerical simulations without devices, and then we average the results separating flood and ebb regimes. The flood regime is defined as all the time periods when the flow goes from West to East, while the ebb regime occurs when the flow goes from East to West. We

Table 1
Main variables for the simulated cases in FVCOM.

Parameter	Value
Turbines diameter (D)	10 m
Hub height (z_{hub})	12 m
Thrust coefficient C_{tFarm}	1.12
Longitudinal disk separation (S_x/D)	5D
Lateral disk separation (S_y/D)	4D
H/z_{hub} case A	4.7
H/z_{hub} case B	5.6
H/z_{hub} case C	6.2
Simulation time	45 days
Bottom roughness (z_0)	40 mm
Grid nodes	4, 164
Sigma layers	10

note that by "upstream of the farm", we refer to the West side of the turbines during the flood regime and the East side of the farm during the ebb regime.

Fig. 8 shows the time-averaged velocities in the zones A, B, and C before incorporating turbine arrays. All results are taken from every zone center span at a distance from the bottom equal to the hub height. In the figure, we observe that for all cases, the average velocity is over 0.7 m/s. As mentioned before, we observe an asymmetry between the ebb and flood regimes; at the edge of the farm zones, all cases have a higher velocity intensity in the ebb regime, however inside the farm case C shows a higher intensity for the flood. Another aspect to notice is that in the flood regime, the C case incidence velocity is more than 12% higher than the other cases; meanwhile, only minor differences among cases exist for the ebb regime.

The direction of the flow is also related to the energy that can be extracted by MHK devices, and the C_{tFarm} coefficient was designed for flows nearly aligned to the turbine axis. Fig. 9 shows the velocity angle before incorporating turbines in the model, where 0° corresponds to a constant latitude. We observe that all the cases have a misalignment of less than 6°, except in case C for the flood regime, which shows a misalignment of around 8°, but this condition is within a reasonable approximation to fully aligned flows with respect to the turbine array [45,46].

In the analysis of the modeled TKE obtained from the turbulence closure, in Fig. 10 we observe points of high intensity, located at the center span of every zone and at the top of the turbine height, since

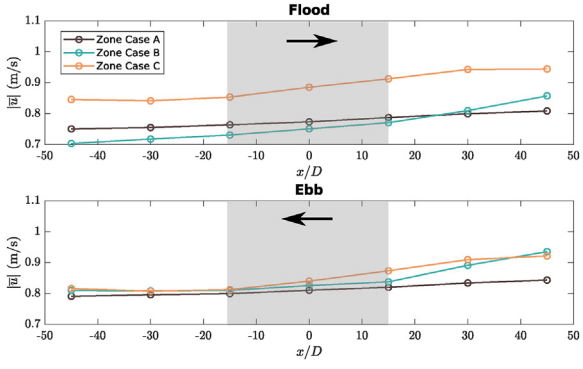

Fig. 8. Absolute velocity in the streamwise direction, u, at the hub height, before simulating turbines in zones A, B, and C (see Fig. 4). The points are at the center span of every zone. In the streamwise direction, the profiles go from 45D (450 m) upstream to the center of the farm location ($x/D = 0$), to 45D (450 m) downstream. The gray areas indicate the location of the farms in the next simulations; meanwhile, the black arrows indicate the flow direction.

these areas are expected to exhibit significant changes when turbines are installed. The figure shows that for the flood regime, case C has the highest TKE, and case A has the lowest; however, in the ebb regime, the opposite occurs. This situation is explained by the bathymetry of the channel that changes significantly the flow structure coming from different sides on each regime, and it is a clear example of a directionally-dependent flow resistance in these tidal channels.

From the FVCOM simulations we can obtain the resolved shear stress at the bed τ_b, as follows:

$$(\tau_{bx}, \tau_{by}) = C_d \sqrt{u^2 + v^2}\ (u, v) \tag{9}$$

where the bottom drag coefficient C_d is determined as:

$$C_d = \max\left(\frac{\kappa^2}{\ln\left(z_{ab}/z_0\right)^2},\ 0.0025\right) \tag{10}$$

here, $\kappa = 0.4$ is the von Kármán constant, and z_0 is the bottom roughness parameter of the bed surface, which is equal to 40 mm in all the simulations [10]. Finally, z_{ab} is the height of the first sigma layer above the bottom, which is around 3 m for the zone A, 3.5 m for the zone B, and 4 m for the zone C. The bed stress τ_b depends on the local velocity and the distance of the first sigma layer from the bed (see equations (9) and (10)). The value of z_0 is obtained from the previous calibration of FVCOM using ADCP data (see Ref. [10] for details). Fig. 11 shows the bottom shear in the flood regime for the three sites with arrays, with differences over 10%, right upstream of the turbine farms. For the ebb regime, however, the differences are much smaller.

4.2. Chacao channel simulations with turbine farms

We present the changes in the flow caused by finite-sized turbine arrays by comparing the cases with devices with the base case. We calculate the absolute change, which is the direct difference between the cases with turbines minus the base case, as well as the percent difference between the results of the simulation. A percentage change equal to 100% means the variable doubles its value with respect to the base case.

In Fig. 12, we show the difference in the velocity with respect to the base case in slices across the center of the turbine array. As expected, we observe a pronounced velocity deficit generated by the turbines in all three cases. The figure shows that the wakes are

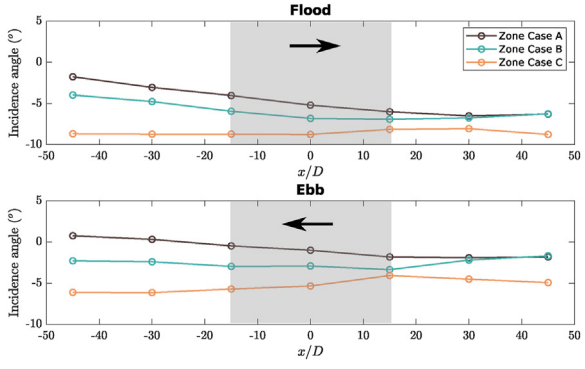

Fig. 9. Incidence angle of velocity at the hub height, before simulating turbines in zones A, B, and C (see Fig. 4). The points are at the center span of every zone. In the streamwise direction, the profiles go from 45D (450 m) upstream to the center of the farm location ($x/D = 0$), to 45D (450 m) downstream. The gray areas indicate the location of the farms in the next simulations; meanwhile, the black arrows indicate the flow direction.

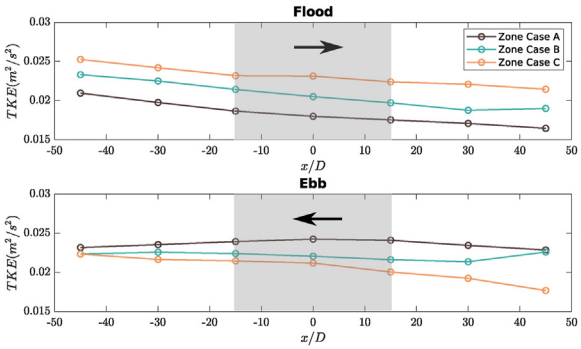

Fig. 10. Modeled TKE obtained from the turbulence model, at a position equivalent to the top turbine height, before simulating turbines in zones A, B, and C (see Fig. 4). The points are at the center span of every zone. In the streamwise direction, the profiles go from 45D (450 m) upstream to the center of the farm location ($x/D = 0$), to 45D (450 m) downstream. The gray areas indicate the location of the farms in the next simulations; meanwhile, the black arrows indicate the flow direction.

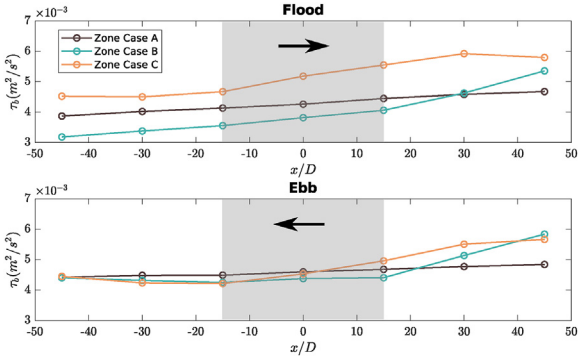

Fig. 11. Bottom shear, τ_b, before simulating turbines in zones A, B, and C (see Fig. 4). The points are at the center span of every zone. In the streamwise direction, the profiles go from 45D (450 m) upstream to the center of the farm location ($x/D = 0$), to 45D (450 m) downstream. The gray areas indicate the location of the farms in the next simulations; meanwhile, the black arrows indicate the flow direction. The shear stress is expressed at the shear-velocity squared $\tau_b/\rho = u_*^2$, which has the same dimensions as the TKE.

different among the cases in direction and magnitude, even though the simulated farm is the same. For example, the wakes for cases A and B are nearly straight; meanwhile, the wakes for case C show a slight deviation of less than 10° for ebb and flood. Additionally, Fig. 12 shows that the cases with higher undisturbed velocity (see Fig. 8) have a higher absolute velocity deficit, which is in agreement with the results of [47].

We also calculate the percent velocity deficit for each case at the hub height, and the farm center span and in Fig. 13, we show that the highest deficit occurs just at the end of the farm for all the cases, and is around 15%–20%. The figure also shows that there are no considerable differences in the percent deficit inside the farms, nor the maximum between the cases. Downstream, Fig. 13 shows that all the cases reach a wake recovery of 95% around 45D to 60D beyond the farm for the flood regime and 50D to 65D for the ebb. In Fig. 13 we can also observe that case A has a higher percent velocity deficit than the other two cases, which means in that case, the velocity takes more distance to recover.

The results for the TKE are quite different than the velocity since the model cannot capture the turbulence increase in the near-wake. However, we can still reproduce the location of the maximum increase and the magnitude beyond 8D downstream [33]. Fig. 14 shows the TKE increase generated by the turbine arrays at the center span and the top of the turbines, where the most significant

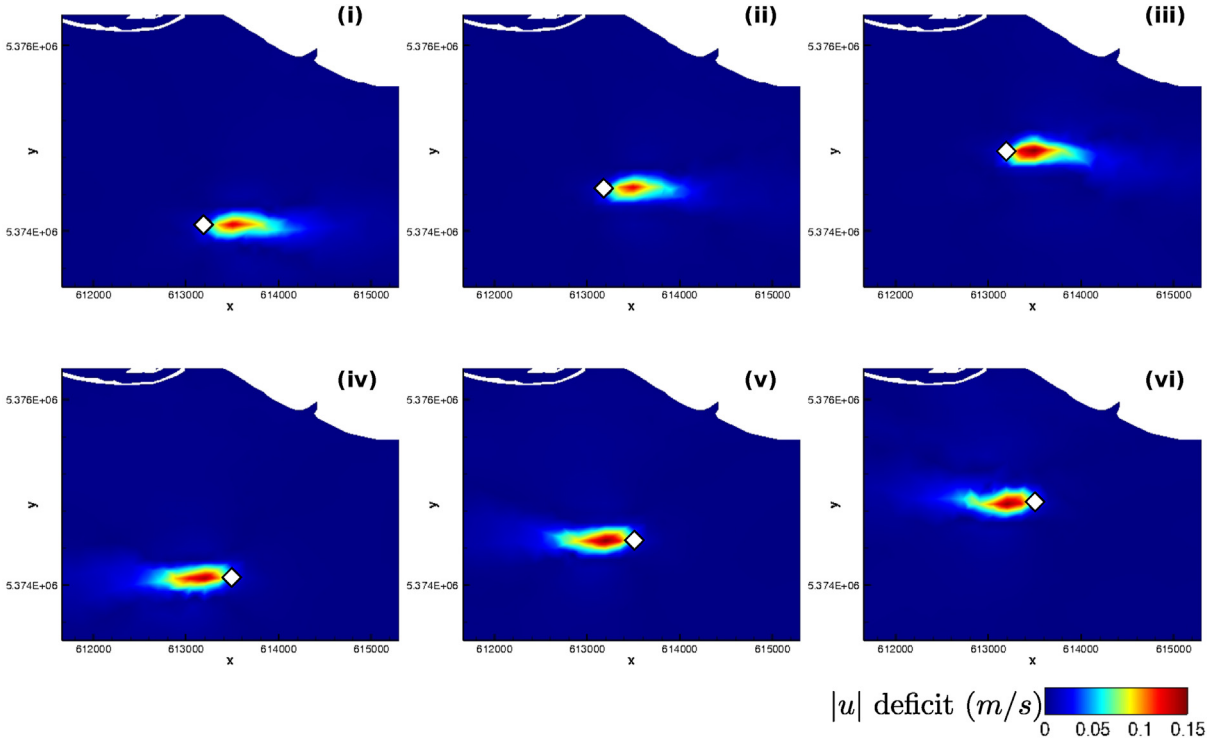

Fig. 12. Slices at farm center colored by the absolute velocity deficit in the streamwise direction, in m/s, with respect to the results of case 0. From left to right, cases A, B, and C, for the flood (top) and ebb (bottom) regimes. White diamonds indicate the center of the farms.

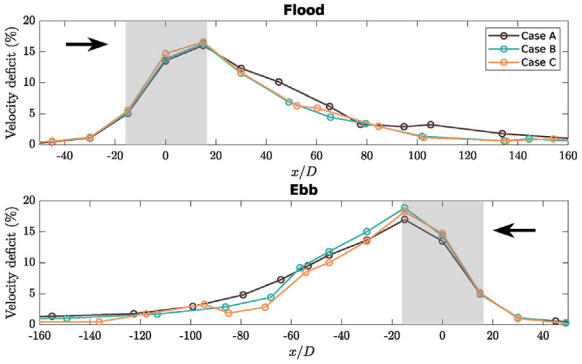

Fig. 13. Percent change the absolute velocity in the streamwise direction, u, at the farm center height due to the device's installation. The points are located at the farm's center span. The position of the farms is highlighted in gray; meanwhile, $x/D = 0$ is the center. The black arrows indicate the flow direction.

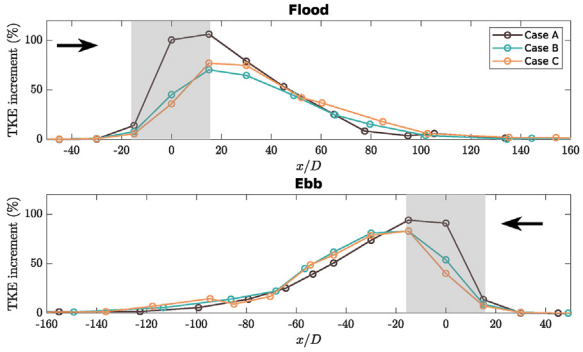

Fig. 14. Percent change the modeled TKE increment at the height of the top turbines due to the device's installation. The points are located at the farm's center span. The position of the farms is highlighted in gray; meanwhile, $x/D = 0$ is the center. The black arrows indicate the flow direction. The 100% are the results of case 0 in the same location as the other cases.

changes occur. This figure shows that the percent TKE increment is considerably higher for case A than for the other cases, in both regimes. This is noteworthy since case A is the zone with the highest initial TKE for flood and the lowest for the ebb, and it also has the largest increment. The results reveal qualitatively the changes and should be taken with caution, as the turbulence model cannot resolve precisely the TKE inside the array, as explained in section 2.1.

Regarding the bottom shear, Fig. 15 shows a positive deficit of τ_b, which has also been seen in other studies [47,48]. The reduction in the bottom shear is a consequence of the velocity reduction in the vicinity of the farms. However, as reported in previous work [33], the bed stresses shows a local increase in the near field captured by 3D models, due to the acceleration of the flow underneath the devices, which cannot be observed in the averaged velocity deficit. To determine if we could resolve this effect, we performed an additional simulation (not shown here) with the same boundary conditions but with a significantly higher vertical resolution to see if we captured any local acceleration, but the results did not produce changes on the vertical profiles of velocity and TKE distributions. These results suggest that different numerical approaches are needed to study scour, which cannot be resolved by OCM at these scales.

In Fig. 15, we also observe that the peak deficit is located at a distance of approximately $15D$ downstream of the turbine array, and case A reaches the maximum deficit of τ_b among all the cases. To study these differences, we compare the TKE near the bottom, whose main source is the shear induced by the bed. In Fig. 16 we show that, unlike the TKE at the top of the turbines, the near-bed kinetic energy decreases with the devices. Particularly, we can

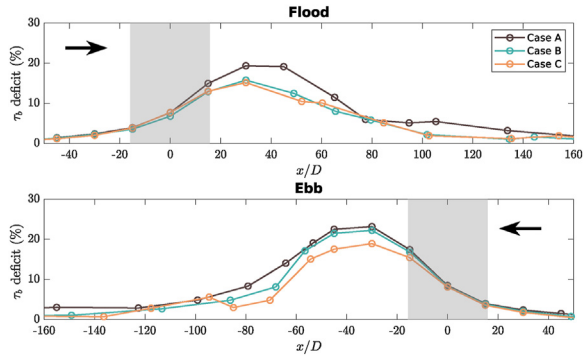

Fig. 15. Bottom shear stress, τ_b, deficit due to the device's installation. The points are located at the farm's center span. The position of the farms is highlighted in gray; meanwhile, $x/D = 0$ is the center. The black arrows indicate the flow direction.

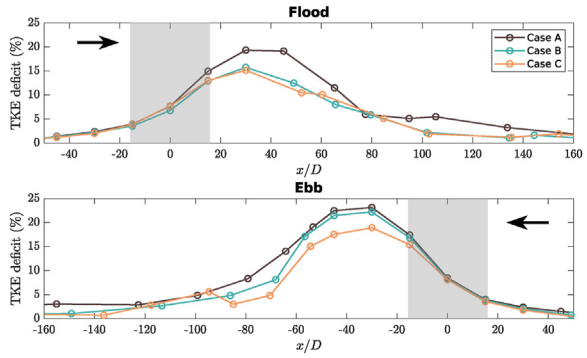

Fig. 16. *TKE* deficit at the bottom due to the device's installation. The points are located at the farm's center span. The position of the farms is highlighted in gray; meanwhile, $x/D = 0$ is the center. The black arrows indicate the flow direction.

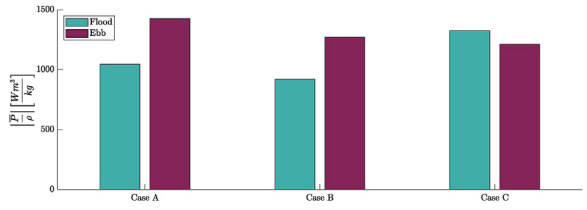

Fig. 17. Theoretical extractable power P of cases A, B, and C, in flood and ebb regime.

observe that in all the cases, the highest TKE deficit downstream of the farm coincides with the location of the highest τ_b deficit.

Finally, we compare the performance of all the cases by calculating the averaged theoretical extractable power P. We compute the momentum difference multiplied by the averaged-velocity in different control volumes around each farm. Fig. 17 shows that the power is more significant in ebb than in flood regime for cases A and B. In case C, howeverm, it is the opposite condition. We also observe that case C has the highest power for the flood regime, and case A has the highest power in the ebb regime. The extractable power is approximately 1 MW, but this estimation does not incorporaye the efficiency of the devices.

5. Discussion

Comparing the base condition with the installation of finite-sized arrays, we observe that the percent change of velocity in the vicinity of the turbines is similar despite the differences in the initial velocity. On the other hand, downstream of the farms we observe that case A has a wake that takes a longer distance to recover, compared to B and C, particularly in flood regime. This coincides with the lower magnitude of the TKE upstream of case A in the flood regime (see Fig. 10), which has a lower impact on the momentum mixing, and consequently a slower wake recovery. We also observe that the initial velocity incident angle also has no relation with the wake downstream the farms, considering that all the cases have a small incident angle, less than 8°. In case C, the incident flow to the turbine array shows a considerable misalignment only for flood regime (see Fig. 9), but the wake has a similar orientation for ebb and flood. In this case, the wake is therefore affected by the proximity to the coastline.

The percent change of TKE increases at the top of the disks because of the shear layer generated by the turbines. This increase of the TKE does not interact with the free surface, due to the depth of the devices in all three cases. We observe that case A has the most elevated percentage TKE increment at this vertical position, since the turbine array is a significant obstacle in a section of the channel with smooth terrain. The TKE magnitude near the bed decreases due to the reduction of the velocity produced by the devices, which also induces lower bed stresses. Inside the arrays, the percent changes of both variables are similar among the cases compared to the base conditions. However, downstream of the farms we observe differences on the wakes: case A has the highest

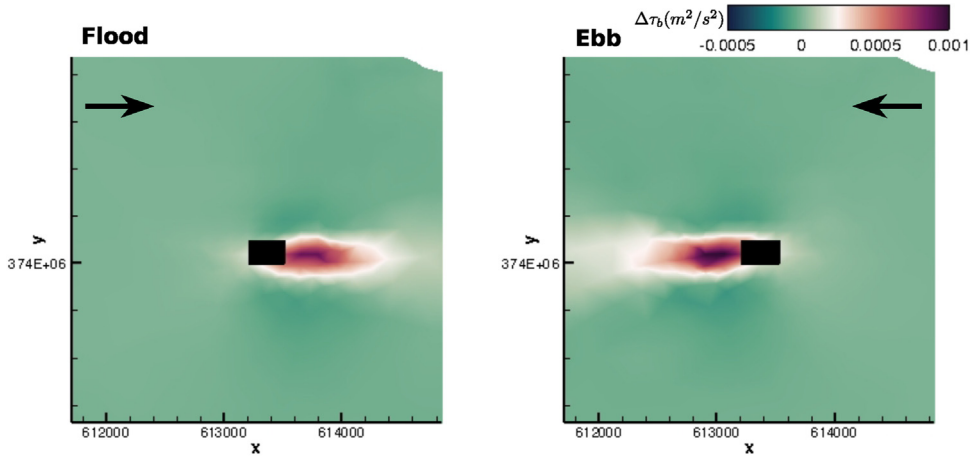

Fig. 18. Difference in the bottom shear, $\Delta\tau_b(m^2/s^2)$, caused by the farm installation in case A, where a positive difference implies a decrease in the bottom shear. Right figure corresponds to the flood regime, and left figure, to the ebb. Black rectangles indicate the area occupied by the turbines; meanwhile the arrows indicates the flow direction.The shear stress is expressed at the shear-velocity squared $\tau_b/\rho = u_*^2$, which has the same dimensions as the TKE.

relative deficit of TKE and bed stresses, and case C has the lowest. We do not observe a relationship between the initial conditions that can explain these differences, but we believe that since smooth bathymetries exert less resistance to the flow near the bottom, the resistance generated by the turbines is more significant than in the rough bathymetry of case C.

To study the changes in the bottom shear it is relevant to predict the modifications on the sediment transport regime induced by the array, which would also require detailed long-term measurements of morphodynamic processes for validation. The spatial distribution and fluctuations of τ_b, however, can be used as representative variable to identify zones are more likely to have erosion and deposition [36]. Fig. 18 shows the difference in the bottom shear of the base case minus the case A, for the flood and ebb regimes. We observe that the turbines would likely cause a sediment deposition downstream the farm that would be more noticeable from the farm ends to around two times the farm size downstream. This is consistent with previous experiments [49], which showed that the sediment is accumulated downstream of two turbines aligned one behind the other; however, they also exhibited erosion in the very near wake (less than $3D$) of the upstream device, which is smaller than our horizontal resolution and it is not captured here, as previously discussed. We also observe in Fig. 18 a slight increase on the bed stresses at the sides of the farms, which would trigger an erosion process in the area.

The theoretical averaged power P of each farm is computed to observe how its magnitude is related to the turbine array location. The results show that power indeed depends directly on the baseline conditions without turbines. The magnitudes of P and TKE show a maximum for case C for flood and in case A for ebb, which are the cases with higher initial TKE for flood and ebb, respectively.

6. Conclusions

In this work, we carried out an analysis of finite-sized turbine arrays in the Chacao channel via numerical simulations of MHK devices using FVCOM coupled with a turbine extension [23]. We incorporated an improved representation of turbine farms by adding an extension to the thrust coefficient, C_{tFarm}, derived from high-resolution numerical simulations [28]. We performed three independent simulations with the same turbine array installed at different locations with different bathymetry features. To ensure a correct resolution of the discretization, we carried out a variogram analysis to identify the predominant lengthscales of the channel bed. The theoretical extractable power was closely related to the magnitude of the inlet velocity, but also with a higher ambient TKE. The percentage change of the other monitored quantities showed that smoother bathymetries can have a considerably higher percent change in TKE and bed shear stresses due to the relative impact that large turbines produce in the flow field. We observed that velocity deficits in sites with smoother bathymetries and low initial TKE takes longer to recover and has a higher percentage increase of TKE at the elevation of the top of the turbine array. At the channel bed we observe that rougher bathymetries with bedform amplitudes of magnitudes around $D/2$ have a lower percentage of τ_b deficit, since the presence of the turbines means less flow resistance than in flatter bathymetries.

With our results, we give new insights and information that will be useful to mitigate the impacts of installing finite-sized farms. Future investigations will focus on other turbine designs, with different tower heights and hub and blade designs, considering also devices installed on floating structures, to predict the effects of the initial conditions and changes on the interactions with bathymetry and waves. We will connect these models with high-resolution simulations, since the understanding of the factors that control the performance of MHK devices and affect the physical environment require to connect models at different scales and resolutions to improve our predictions.

CRediT authorship contribution statement

Karina Soto-Rivas: Conceptualization, Methodology, Software, Writing – original draft, Writing – review & editing. **David Richter:** Conceptualization, Methodology, Writing – original draft, Supervision, Writing – review & editing. **Cristian Escauriaza:** Conceptualization, Methodology, Writing – original draft, Supervision, Writing – review & editing.

Declaration of competing interest

The authors declare that they have no known competing financial interests or personal relationships that could have appeared to influence the work reported in this paper.

Acknowledgements

This work has been supported by the Marine Energy Research & Innovation Center of Chile (MERIC) CORFO project 14CEI2-28228, and Fondecyt project 1191785. Computational resources were provided by the support of supercomputing infrastructure of the NLHPC (ECM-02) and Research Internationalization Grant of the Pontificia Universidad Católica de Chile (grant no. PUC1566).

References

[1] A. Badcock-Broe, R. Flynn, S. George, R. Gruet, N. Medic, Wave and tidal energy market deployment strategy for europe, Tech. rep, in: Strategic Initiative for Ocean Energy, 2014. URL, https://www.oceanenergy-europe.eu/wp-content/uploads/2017/10/SI_Ocean_Market_Deployment_Strategy_-_Web_version.pdf.
[2] M. Chowdhury, K.S. Rahman, V. Selvanathan, N. Nuthammachot, M. Suklueng, A. Mostafaeipour, A. Habib, M. Akhtaruzzaman, N. Amin, K. Techato, Current trends and prospects of tidal energy technology, Environment, Dev. Sustain. (2020) 1–16, https://doi.org/10.1007/s10668-020-01013-4.
[3] T.A. Adcock, S. Draper, R.H. Willden, C.R. Vogel, The fluid mechanics of tidal stream energy conversion, Annu. Rev. Fluid Mech. 53 (2021) 287–310.
[4] J. Ladenburg, A. Dubgaard, Willingness to pay for reduced visual disamenities from offshore wind farms in Denmark, Energy Pol. 35 (8) (2007) 4059–4071, https://doi.org/10.1016/j.enpol.2007.01.023.
[5] J. Ladenburg, A. Dubgaard, Preferences of coastal zone user groups regarding the siting of offshore wind farms, Ocean Coast Manag. 52 (5) (2009) 233–242, https://doi.org/10.1016/j.ocecoaman.2009.02.002. URL, https://www.sciencedirect.com/science/article/pii/S0964569109000180.
[6] M. Voke, I. Fairley, M. Willis, I. Masters, Economic evaluation of the recreational value of the coastal environment in a marine renewables deployment area, Ocean Coast Manag. 78 (2013) 77–87, https://doi.org/10.1016/j.ocecoaman.2013.03.013. URL, https://www.sciencedirect.com/science/article/pii/S096456911300080X.
[7] M. De Dominicis, R.O. Murray, J. Wolf, Multi-scale ocean response to a large tidal stream turbine array, Renew. Energy 114 (2017) 1160–1179, https://doi.org/10.1016/j.renene.2017.07.058.
[8] G. Deng, Z. Zhang, Y. Li, H. Liu, W. Xu, Y. Pan, Prospective of development of large-scale tidal current turbine array: an example numerical investigation of Zhejiang, China, Appl. Energy 264 (2020), 114621.
[9] Gobierno de Chile, Chile's nationally determined contribution (NDC), URL, https://mma.gob.cl/wp-content/uploads/2020/04/Chiles_NDC_2020_english.pdf.
[10] M. Guerra, R. Cienfuegos, J. Thomson, L. Suarez, Tidal energy resource characterization in Chacao Channel, Chile, Int. J. Mar. Energy 20 (2017) 1–16, https://doi.org/10.1016/j.ijome.2017.11.002.
[11] I. Fairley, I. Masters, H. Karunarathna, The cumulative impact of tidal stream turbine arrays on sediment transport in the Pentland Firth, Renew. Energy 80 (2015) 755–769, https://doi.org/10.1016/j.renene.2015.03.004.
[12] A.J.G. Brown, S.P. Neill, Hydrodynamic response to large scale tidal energy extraction, in: European Wave and Tidal Energy Conference 2015, 2015.
[13] M. Garcia-Oliva, S. Djordjević, G.R. Tabor, The influence of channel geometry on tidal energy extraction in estuaries, Renew. Energy 101 (2017) 514–525, https://doi.org/10.1016/j.renene.2016.09.009.

[14] D.R. Plew, C.L. Stevens, Numerical modelling of the effect of turbines on currents in a tidal channel – tory channel, New Zealand, Renew. Energy 57 (2013) 269–282, https://doi.org/10.1016/j.renene.2013.02.001.
[15] D. Fallon, M. Hartnett, A. Olbert, S. Nash, The effects of array configuration on the hydro-environmental impacts of tidal turbines, Renew. Energy 64 (2014) 10–25, https://doi.org/10.1016/j.renene.2013.10.035.
[16] S. Nash, N. O'Brien, A. Olbert, M. Hartnett, Modelling the far field hydro-environmental impacts of tidal farms – a focus on tidal regime, inter-tidal zones and flushing, Computers & Geosciences, Mar. Renew. Energy 71 (2014) 20–27, https://doi.org/10.1016/j.cageo.2014.02.001.
[17] S.P. Neill, J.R. Jordan, S.J. Couch, Impact of tidal energy converter (tec) arrays on the dynamics of headland sand banks, Renew. Energy 37 (1) (2012) 387–397, https://doi.org/10.1016/j.renene.2011.07.003.
[18] A. Shchepetkin, J. McWilliams, The regional oceanic modeling system (ROMS): oceanic model, Ocean Model. 9. doi:10.1016/j.ocemod.2004.08.002.
[19] T. Roc, D. Conley, D. Greaves, Methodology for tidal turbine representation in ocean circulation model, Renew. Energy 51 (2013) 448–464, https://doi.org/10.1016/j.renene.2012.09.039.
[20] A.J. Goward Brown, S.P. Neill, M.J. Lewis, Tidal energy extraction in three-dimensional ocean models, Renewable Energy, Wave Tidel Res. Char. 114 (2017) 244–257, https://doi.org/10.1016/j.renene.2017.04.032.
[21] C. Chen, H. Liu, R.C. Beardsley, An unstructured grid, finite-volume, three-dimensional, primitive equations ocean model: application to coastal ocean and estuaries, J. Atmos. Ocean. Technol. 20 (1) (2003) 159–186, https://doi.org/10.1175/1520-0426(2003)020. <0159:AUGFVT>2.0.CO;2.
[22] Z. Yang, T. Wang, A.E. Copping, Modeling tidal stream energy extraction and its effects on transport processes in a tidal channel and bay system using a three-dimensional coastal ocean model, Renew. Energy 50 (2013) 605–613, https://doi.org/10.1016/j.renene.2012.07.024.
[23] R.O. Murray, A. Gallego, A modelling study of the tidal stream resource of the Pentland Firth, Scotland, Renew. Energy 102 (2017) 326–340, https://doi.org/10.1016/j.renene.2016.10.053.
[24] Z. Yang, T. Wang, A. Copping, S. Geerlofs, Modeling of in-stream tidal energy development and its potential effects in Tacoma Narrows, in: Science in Support of Governance of Wave and Tidal Energy Developments, vol. 99, Ocean and Coastal Management, Washington, USA, 2014, pp. 52–62, https://doi.org/10.1016/j.ocecoaman.2014.02.010.
[25] T. Wang, Z. Yang, A modeling study of tidal energy extraction and the associated impact on tidal circulation in a multi-inlet bay system of Puget Sound, Renewable Energy, Wave Tidel Res. Char. 114 (2017) 204–214, https://doi.org/10.1016/j.renene.2017.03.049.
[26] L. Myers, A. Bahaj, An experimental investigation simulating flow effects in first generation marine current energy converter arrays, Renew. Energy 37 (2012) 28–36, https://doi.org/10.1016/j.renene.2011.03.043.
[27] J. Riglin, C. Daskiran, J. Jonas, W.C. Schleicher, A. Oztekin, Hydrokinetic turbine array characteristics for river applications and spatially restricted flows, Renew. Energy 97 (2016) 274–283, https://doi.org/10.1016/j.renene.2016.05.081. URL, http://www.sciencedirect.com/science/article/pii/S0960148116304918.
[28] K. Soto-Rivas, D. Richter, C. Escauriaza, A formulation of the thrust coefficient for representing finite-sized farms of tidal energy converters, Energies 12 (20) (2019) 3861, https://doi.org/10.3390/en12203861.
[29] D.M. Mark, P.B. Aronson, Scale-dependent fractal dimensions of topographic surfaces: an empirical investigation, with applications in geomorphology and computer mapping, J. Int. Assoc. Math. Geol. 16 (7) (1984) 671–683, https://doi.org/10.1007/BF01033029.
[30] T. Burton, D. Sharpe, N. Jenkins, E. Bossanyi, Wind Energy Handbook, John Wiley & Sons, Ltd, Baffins Lane, Chichester West Sussex, PO19 1UD, England, 2011, ISBN 0-471-48997-2.
[31] J. Sandoval, K. Soto-Rivas, C. Gotelli, C. Escauriaza, Modeling the wake dynamics of a marine hydrokinetic turbine using different actuator representations, Ocean Eng. 222 (2021), 108584.
[32] G.L. Mellor, T. Yamada, Development of a turbulence closure model for geophysical fluid problems, Rev. Geophys. 20 (4) (1982) 851–875, https://doi.org/10.1029/RG020i004p00851.
[33] X. Li, M. Li, S.J. McLelland, L.-B. Jordan, S.M. Simmons, L.O. Amoudry, R. Ramirez-Mendoza, P.D. Thorne, Modelling tidal stream turbines in a three-dimensional wave-current fully coupled oceanographic model, Renew. Energy 114 (2017) 297–307, https://doi.org/10.1016/j.renene.2017.02.033.
[34] S. Paboeuf, P. Yen Kai Sun, L.-M. Macadré, G. Malgorn, Power performance assessment of the tidal turbine Sabella D10 following iec62600-200, in: Ocean Space Utilization; Ocean Renewable Energy of International Conference on Offshore Mechanics and Arctic Engineering, vol. 6, 2016, https://doi.org/10.1115/OMAE2016-54836.
[35] D. C. Preziuso, R. S. O'Neil, M. J. E. Alam, D. Bhatnagar, S. Bhattacharya, S. Ganguli, Y.-H. Yu, G. Stark, Understanding the Grid Value Proposition of Marine Energy: A Literature Review.
[36] C. Gotelli, M. Musa, M. Guala, C. Escauriaza, Experimental and numerical investigation of wake interactions of marine hydrokinetic turbines, Energies 12 (16) (2019) 3188.
[37] C. D. Markfort, W. Zhang, F. Porté-Agel, Turbulent flow and scalar transport through and over aligned and staggered wind farms, J. Turbul. 13 (33). doi:10.1080/14685248.2012.709635.
[38] Y.-T. Wu, F. Porté-Agel, Simulation of turbulent flow inside and above wind farms: model validation and layout effects, Boundary-Layer Meteorol. 146 (2) (2013) 181–205, https://doi.org/10.1007/s10546-012-9757-y.
[39] C. Daskiran, J. Riglin, A. Oztekin, Computational study of multiple hydrokinetic turbines: the effect of wake, in: ASME International Mechanical Engineering Congress and Exposition, vol. 57465, American Society of Mechanical Engineers, 2015. V07AT09A021.
[40] D.M. O'Doherty, A. Mason-Jones, C. Morris, T. O'Doherty, C. Byrne, P.W. Prickett, R.I. Grosvenor, Interaction of marine turbines in close proximity, in: 9th European Wave and Tidal Energy Conference (EWTEC), 2011, pp. 10–14. Southampton, UK.
[41] C. Escauriaza, F. Sotiropoulos, Initial stages of erosion and bed form development in a turbulent flow around a cylindrical pier, J. Geophys. Res.: Earth Surf. 116 (F03007). doi:10.1029/2010JF001749.
[42] E. Gringarten, C.V. Deutsch, Teacher's aide variogram interpretation and modeling, Math. Geol. 33 (4) (2001) 507–534, https://doi.org/10.1023/A:1011093014141.
[43] G. Artan, C. Neale, D. Tarboton, Characteristic length scale of input data in distributed models: implications for modeling grid size, J. Hydrol. 227 (1) (2000) 128–139, https://doi.org/10.1016/S0022-1694(99)00176-6. URL, https://www.sciencedirect.com/science/article/pii/S0022169499001766.
[44] Z. Mohammadi, Variogram-based approach for selection of grid size in groundwater modeling, Appl. Water Sci. 3 (2013) 597–602, https://doi.org/10.1007/s13201-013-0107-0.
[45] C. Frost, P. Evans, M. Harrold, A. Mason-Jones, T. O'Doherty, D. O'Doherty, The impact of axial flow misalignment on a tidal turbine, Renew. Energy 113 (2017) 1333–1344, https://doi.org/10.1016/j.renene.2017.07.006.
[46] M. Musa, G. Ravanelli, W. Bertoldi, M. Guala, Hydrokinetic turbines in yawed conditions: toward synergistic fluvial installations, J. Hydraul. Eng. 146 (4) (2020), 04020019, https://doi.org/10.1061/(ASCE)HY.1943-7900.0001707.
[47] N. Guillou, J. Thiébot, The impact of seabed rock roughness on tidal stream power extraction, Energy 112 (2016) 762–773, https://doi.org/10.1016/j.energy.2016.06.053.
[48] J. Thiébot, P.B. du Bois, S. Guillou, Numerical modeling of the effect of tidal stream turbines on the hydrodynamics and the sediment transport – application to the Alderney Race (Raz Blanchard), France, Renew. Energy 75 (2015) 356–365, https://doi.org/10.1016/j.renene.2014.10.021.
[49] C. Hill, M. Musa, M. Guala, Interaction between instream axial flow hydrokinetic turbines and uni-directional flow bedforms, Renew. Energy 86 (2016) 409–421, https://doi.org/10.1016/j.renene.2015.08.019.